# Intrinsic bipolar membrane characteristics dominate the effects of flow orientation and external pH-profile on the membrane voltage

Sharifian, R.; Blommaert, M. A.; Bremer, M.; Wagterveld, R. M.; Vermaas, D. A.

**DOI**
10.1016/j.memsci.2021.119686

**Publication date**
2021

**Document Version**
Final published version

**Published in**
Journal of Membrane Science

**Citation (APA)**
Sharifian, R., Blommaert, M. A., Bremer, M., Wagterveld, R. M., & Vermaas, D. A. (2021). Intrinsic bipolar membrane characteristics dominate the effects of flow orientation and external pH-profile on the membrane voltage. *Journal of Membrane Science*, *638*, Article 119686. https://doi.org/10.1016/j.memsci.2021.119686

Journal of Membrane Science 638 (2021) 119686

Contents lists available at ScienceDirect

Journal of Membrane Science

journal homepage: www.elsevier.com/locate/memsci

# Intrinsic bipolar membrane characteristics dominate the effects of flow orientation and external pH-profile on the membrane voltage

R. Sharifian [a,b], M.A. Blommaert [a], M. Bremer [b], R.M. Wagterveld [b], D.A. Vermaas [a,*]

[a] Department of Chemical Engineering, Faculty of Applied Sciences, Delft University of Technology, the Netherlands
[b] Wetsus, European Centre of Excellence for Sustainable Water Technology, Leeuwarden, the Netherlands

ARTICLE INFO

*Keywords:*
Bipolar membrane
Voltage
pH profile
Water dissociation reaction
Flow orientation
Energy consumption

ABSTRACT

The practical energy required for water dissociation reaction in bipolar membrane (BPM) is still substantially higher compared to the thermodynamic equivalent. This required energy is determined by the bipolar membrane voltage, consisting of (1) thermodynamic potential and (2) undesired voltage losses. Since the pH gradient over the BPM affects both voltage components, in this work, pH gradient is leveraged to decrease the BPM-voltage. We investigate the effect of four flow orientations: 1) co-flow, 2) counter-flow, 3) co-recirculation, and 4) counter-recirculation, on the pH gradient and BPM-voltage, using an analytical model and chronopotentiometry experiments. The analytical model predicts the experimentally obtained pH accurately and confirms the importance of the flow orientation in determining the longitudinal pH gradient profile over the BPM in the bulk solution. However, in contrast to the simulated results, our observations show the effect of flow orientations on the BPM-voltage to be insignificant under practical operating conditions. When the water dissociation reaction in the BPM is dominant, the internal local pH inside of the membrane determines its final voltage, shadowing the effect of the external pH-gradient in the bulk solution. Therefore, although changing the flow orientation affects the bulk pH, it does not influence the local pH at the BPM junction layer and hence the BPM-voltage. Instead, opportunities for reducing the membrane voltage are in the realm of improved catalysts and ion exchange layers of the BPM.

## 1. Introduction

As industry and society is transitioning to sustainable electrified technologies, electrochemical methods are becoming more and more attractive. Bipolar membranes (BPM) have been successfully utilized in (emerging) electrochemical systems to create, and sustain, different pH at membrane's either sides. The BPM-facilitated applications range from concentrated acid/base production [1], organic synthesis, biotechnology/food industry [2,3], production of value-added products [4–10], energy storage/conversion [11,12], resource recovery [13] (like $CO_2$ capture [14–19] and ammonia recovery [20–22]), and electrolysers [23–25]. A bipolar membrane consists of an anion and a cation exchange layer (AEL and CEL) laminated together. Upon application of an electrical current, inside of the BPM, water dissociation reaction (WDR) takes place in a "reverse bias mode" (i.e., CEL facing the cathode). The BPM provides, ideally, an impermeable barrier for salt ions from the electrolyte to cross the bipolar membrane (BPM). Instead, through the water dissociation reaction, the BPM produces $H^+$ and $OH^-$ ions. The water dissociation reaction enables a pH gradient over the bipolar membrane ($\Delta pH_{BPM}$) without the necessity of forming (gaseous) by-products.

Despite the advances made in BPMs, the energy consumption in BPM-facilitated applications, for water dissociation, is still high. The thermodynamic contribution of the BPM-voltage (i.e., reversible voltage, $V_{rev}$) is proportional to the pH difference and is only 0–0.83 V for pH-gradient between 0 and 14. However, the actual BPM-voltage is often measured beyond 1 V at any industrially relevant current density [5,24,26,27]. In addition to thermodynamics, kinetics of water splitting, determined by its catalyst, is crucial in determining the actual BPM-voltage [28]. Manufacturing a properly catalyzed BPM, with highly permselective ion-exchange layers (i.e., perfect co-ion exclusion) and with optimum (layers/catalyst) thickness is the most direct way to minimize energy losses [27]. Additionally, as the thermodynamic reversible voltage ($V_{rev}$) is only dependent on the magnitude of ΔpH over the BPM, controlling the pH difference over the membrane is a potential lever to control the total BPM-voltage ($V_{BPM}$) independent of

* Corresponding author.
*E-mail address:* d.a.vermaas@tudelft.nl (D.A. Vermaas).

https://doi.org/10.1016/j.memsci.2021.119686
Received 9 April 2021; Received in revised form 31 July 2021; Accepted 1 August 2021
Available online 10 August 2021

the membrane manufacturing. The effect of various feed pH on $V_{BPM}$ has been demonstrated previously for cells that have a uniform pH in the feed compartment along the flow direction [5,27,29]. It has also been numerically shown that the external pH gradient (i.e., $\Delta pH_{BPM}$ of the feed solutions) over the BPM affects the ion concentration profile inside the BPM [27]. According to the mass balance, changing the hydrodynamic factors such as the flow orientation along the BPM affects the pH gradient profile over the BPM, which suggests that the flow orientation impacts the BPM voltage. However, the effect of flow orientations on the pH gradient profile along the BPM, and its subsequent impact on the BPM-voltage are still missing.

Although the effect of different flow modes in bipolar membrane applications is missing in the literature, the performance of co-flow and counter-flow modes is studied before in electrodialysis (ED) and reverse electrodialysis (RED) cells containing monopolar membranes [30,31]. In RED, simulations demonstrate that counter-flow allows almost twice higher efficiencies in electricity production compared to the co-flow, due to lower ohmic losses and less untapped energy [31]. In comparison with RED and ED, the flow orientation has potentially even more impact in BPM-based processes when using solutions with initially mild pH, because the concentration difference of $H^+$ (and $OH^-$) ions over the membrane is easily multiple orders of magnitude larger at the outflow of the cell compartments compared to the inflow. The co-flow and counter-flow orientations can be applied in all BPM-based applications. The recirculation modes are suitable for resource recovery e.g., $CO_2$ capture [32], ammonia and phosphorous recovery [22,33], where after the extraction step, the acidic stream can be recirculated in the base compartment, enabling a neutral outflow.

This work represents BPM-facilitated technologies that deal with a mild pH, since the pH (and thus the theoretical $V_{rev}$) is insensitive to flow orientation at extreme pH. The targeted setup covers typical circumstances for e.g., electrochemical $CO_2$ capture/conversion and resource recovery. We investigate the effect of different flow orientations on the reversible voltage ($V_{rev}$) and irreversible losses ($V_{irr}$) in bipolar membrane electrodialysis (BPMED), aiming to decrease the energy required by the BPM. First, a theoretical model is used to calculate the pH profile and $V_{rev}$ over the BPM, using the mass balance and Visual MINTEQ ver. 3.1 chemical equilibrium software. Subsequently, BPM-voltage and its components are measured through chronopotentiometry experiments in a six-compartment BPMED cell. Finally, we share understanding of the involved losses in the system and give guidelines to reduce the currently high energy consumption in BPM-facilitated applications through membrane manufacturing.

## 2. Theory

### 2.1. BPM-voltage ($V_{BPM}$)

The BPM-voltage consists of two main components: (1) the thermodynamic (reversible) voltage required for water dissociation and (2) the undesired losses. When the current density is sufficiently high for water dissociation reaction to be the main charge carrier across the BPM, the reversible voltage can be defined using the Nernst equation [5,26,34,35]:

$$V_{rev} = \frac{\Delta G}{nF} = 0.059 \Delta pH_{BPM} \quad (1)$$

Where $\Delta G$ is the Gibbs free energy that is required for acid and base production in an ideal bipolar membrane (i.e., complete exclusion of any ions except $H^+$ and $OH^-$) at ambient temperature and pressure (J). $V_{rev}$ is the thermodynamic reversible voltage across the BPM (V), F Faraday constant (C $mol^{-1}$), n number moles of electrons transferred in the reaction, and $\Delta pH_{BPM}$ the pH-difference between the AEL-electrolyte and CEL-electrolyte interfaces of the BPM.

The losses can be approximated as [28,34–36]:

$$V_{irr}^{BPM} \approx \ iR_M + \eta_{WDR} \quad (2)$$

Where $R_M$ (= $R_{layers,\ stat}$) represents the membrane Ohmic area resistivity ($\Omega\ cm^2$) in the steady state, $\eta_{WDR}$ the overpotential of the water dissociation reaction (V) [36–39], and i the applied current density (A $cm^{-2}$) [36]. Additional voltage losses, such as the water transport limitations from the electrolyte towards the BPM junction layer (JL) are neglected in Equation (2) [28,40,41].

### 2.2. pH-gradient in z-axis over the BPM ($\Delta pH_{BPM}$)

The longitudinal pH-gradient can be obtained via the mass balance equation [34]. Assuming the AEM and the CEM are impermeable to co-ions, the mass balance can be written as (see also illustration of fluxes in Fig. 1 A):

$$C_{outflow}^{H^+} = C_{inflow}^{H^+} + J_{H^+}\frac{A_m}{q} \quad (3)$$

$$J_{H^+} = \frac{i}{z_{H^+}\ F} \quad (4)$$

$$C_{outflow}^{H^+} = C_{inflow}^{H^+} + \frac{i}{z_{H^+}\ F}\frac{t_r}{d} \quad (5)$$

Where subscripts inflow (i.e., at z = 0) and outflow (i.e., at z = L = length of the cell) indicate the solution that flows in and out of the cell compartment, respectively. $C_{inflow}^{H^+}$ and $C_{outflow}^{H^+}$ (mol $m^{-3}$) represent the total acidity, meaning that the include (1) the free $H^+$ ions plus (2) the protons present in complexes in case of a buffered solution is used. $A_m$ is the active area of the bipolar membrane ($m^2$), i the applied current density (A $m^{-2}$), $J_{H^+}$ the flux of produced $H^+$ ions from the BPM (mol $m^{-2}s^{-1}$), $z_{H^+}$ the electrochemical valence (=1 for $H^+$ ion), d the compartment thickness (m) and q the flow rate ($m^3\ s^{-1}$), where

$$q = \frac{V_{acid}}{t_r} = \frac{A_m\ d}{t_r}$$

with $V_{acid}$ being the acidic compartment volume in $m^3$ (here, $V_{acid}$ = $V_{base}$) and $t_r$ the cell residence time (s). The term $\frac{i}{z_{H^+}\ F}\frac{t_r}{d}$ (mol $m^{-3}$) quantifies the produced moles of $H^+$ ions from the water dissociation reaction, per volume of the acidic compartment (if 100% Coulombic efficiency is assumed).

To calculate the pH from $C_{inflow}^{H^+}$ and $C_{outflow}^{H^+}$, in an unbuffered solution:

$$C_{inflow}^{H^+} = 10^{-pH_{inflow}}, C_{outflow}^{H^+} = 10^{-pH_{outflow}} \quad (6)$$

However, depending on the buffer capacity, part of the produced $H^+$ ions from the water dissociation reaction neutralize with buffer compounds and, hence, will not contribute to a pH change. For example, in the phosphate buffer system:

$$10^{-pH} = C^{H^+} - \left(\left[HPO_4^{2-}\right] + 2\cdot\left[H_2PO_4^-\right] + 3\cdot\left[H_3PO_4\right]\right) \quad (7)$$

Using Equations (5)–(7), the acidic and basic $pH_{outflow}$ can be calculated at each current density (i), compartment thickness (d), and cell residence time ($t_r$). Alternatively, by keeping i, d and $t_r$ constant and by varying in z-axis between 0 and L, the full pH profile inside of the cell, in the direction of the flow, is obtainable through a stepwise mass balance at each position along the flow direction (z-axis):

$$C_{l_i}^{H^+} = C_{l_{i-1}}^{H^+} + \frac{z_i - z_{i-1}}{L}\left(\frac{i}{F}\frac{t_r}{d}\right) \quad \text{for } 0 < \ z_i \le L \quad (8)$$

L is the total length of the cell in the direction of the flow (z-axis in Fig. 1). In Equation (8) subscript i indicates the $i^{th}$ length step chosen for the stepwise mass balance.

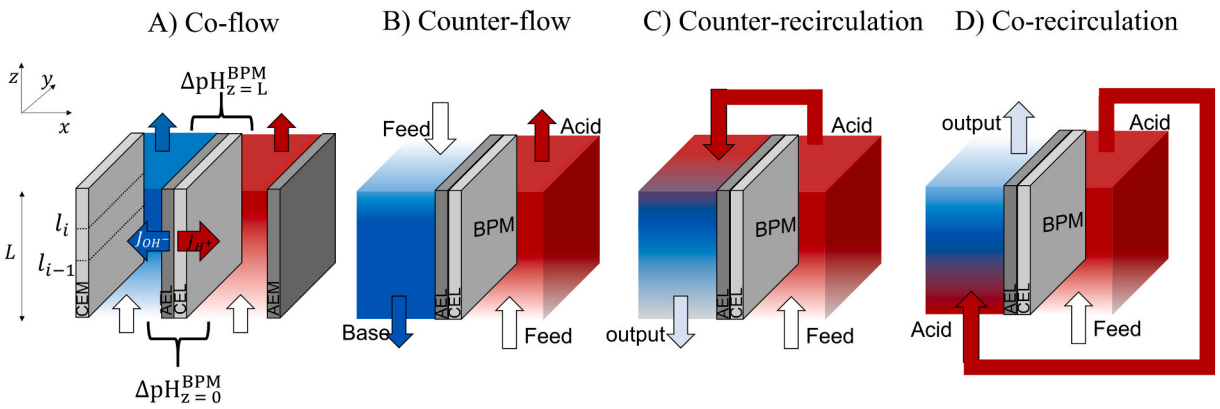


**Fig. 1.** Schematic of the four flow orientation modes and $H^+$ ion mass balance. L represents the compartment length in z-axis.

## 3. Materials and methods

Three solutions of 0.5 M NaCl, 0.5 M NaCl +2.5 mM $NaHCO_3$, and 0.45 M NaCl +50 mM $Na_2HPO_4$ were used in four flow orientations according to Fig. 1 A-D. The chosen solutions mimic an unbuffered reference case, seawater (to represent the oceanic $CO_2$ capture application of BPMED), and industrial water, respectively. The choice for the concentration of the phosphate (and NaCl) is to ensure similar neutral initial pH (and ionic conductivity) for all the three solutions. The buffer capacity and the underlying equilibrium that control the concentration of total and free $H^+$ ions are calculated using Equations (5)–(8) and with Visual MINTEQ ver. 3.1 as explained in the SI.

### 3.1. BPMED setup

A single cell (i.e., 1 repeating unit) BPMED setup was assembled (Fig. S1), using six compartments to avoid interference between electrodes and acid/base compartments. The setup comprised 22 $cm^2$ FBM-130, FKB-PK-130 and FAB-PK-130 (FuMATech B.V.) as the BPM, CEM and AEM membranes, respectively. The compartment thickness (i.e., distance between the membranes) was d = 1 cm, and the cell length (in z-direction) was L = 11 cm. Prior to each run, all membranes used were equilibrated for several hours with 0.5 M NaCl and the cell was washed with demineralized water. All salts were acquired from VWR (purity of >99.7%). To avoid $CO_2$(g) bubbles upon acidification of 0.5 M NaCl + 2.5 mM $NaHCO_3$ [42], a membrane contactor (3 M™ Liqui-Cel™ MM Series 8.75 inch) was placed after the outflow (z = L) of the acidic compartment [19] and before recirculation to the base compartment in both recirculation modes. No gas bubbles were visibly trapped during any of the experiments (for any of the three tested solutions).

The feed solutions were pumped through the cell at flow rate of 30 ml $min^{-1}$ (i.e., flow velocity of 0.25 cm $s^{-1}$, $t_r$ = 44 s) by peristaltic pumps (Cole-Parmer, Masterflex L/S Digital drive).

### 3.2. Applied techniques

Chronopotentiometry experiments were performed using an Ivium Potentiostat (Ivium Technologies B.V.) in a four-electrode setup, measuring the BPM-voltage through two leak-free Ag–AgCl (sat. KCl) reference electrodes (Innovative Instruments, Inc.), placed in situ at two sides of the membrane (at z = 0.5L). The distance between the reference electrodes was approximately 1 cm, and the BPM was placed exactly between these electrodes. The pH and temperatures (always 23 ± 2 °C) were monitored in line with Orbisint CPS11D-7BA21 pH probes connected to a Liquiline CM444, both from Endress + Hauser (Germany).

Current densities of 5, 12.5, and 25 mA $cm^{-2}$ were applied for 20 min at a recording interval of 2 s. After applying the current, the BPM-voltage ($V_{BPM}$) stabilized for all series within couple of minutes (<200 s). The steady-state values of $V_{BPM}$ (at z = 0.5 L) and the outflow acidic and basic pH (at z = L), averaged over the last (stable) 5 min of the constant current interval, were used for processing. However, the pH of the base output for 0.5 M NaCl co-recirculation and counter-recirculation fluctuated in all repetitions (Figure S5 C-D). This is while the BPM-voltage reached steady-state within couple of seconds after applying the current. As the mentioned pH-fluctuations were not progressing with time, same averaging interval was applied for these cases.

### 3.3. Measuring reversible and irreversible voltages

The reversible and irreversible voltage contributions of the BPM-voltage can be obtained through chronopotentiometry (Fig. 2) [43]. When the current is switched on (at $t_{on}$), both the solution (between the two sides of the membrane and the tips of the reference electrodes) and the membrane layers resistances contribute to the initially measured electric potential drop ($V_{ohm}$ in Fig. 2) [43]:

$$V_{ohm} = V_{sol} + V_{mem,\ ini} = I\ \left(R_{sol} + R_{mem,\ ini}\right) \quad (9)$$

Where $R_{sol}$ (Table S1) and $R_{mem,\ ini}$ represent the solution and the initial BPM-layers ohmic resistances (Ω).

The irreversible voltage contributions ($V_{irr}$) can be derived from the sudden drop in voltage directly after turning off the constant current (at $t_{off}$). The membrane resistance in steady state (Equation (2)), will differ from the initial resistance ($R_{mem,\ ini}$ in Equation (9)) because of the difference in the concentration profiles and additional ionic species in the membrane layers due to the current application [43].

The reversible potential ($V_{rev}$) is the electrical potential remaining after switching off the power supply (Fig. 2) [39]. $V_{rev}$ relates to the water dissociation reaction in the membrane and the concentration differences over the BPM-layers [43]. For current densities above the

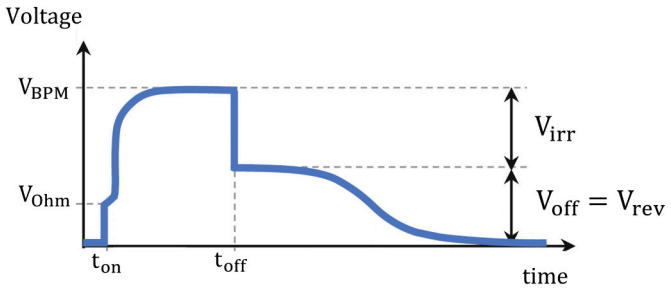


**Fig. 2.** Schematic representation of a typical chronopotentiometry curve when the water dissociation reaction is dominant. The $t_{on}$ and $t_{off}$ mark the period of constant current application. The total steady state BPM-voltage ($V_{BPM}$) is the summation of the reversible voltage and irreversible voltage losses: $V_{BPM} = V_{rev} + V_{irr}$.

limiting current density, when the water dissociation reaction in the BPM is dominant over the salt ion-crossover, $V_{rev}$ can be represented based on the concentration differences of $H^+$ and $OH^-$ over the BPM junction and membrane-electrolyte interfaces, which is described in Equation (1) for an ideal BPM. This potential diminishes as the ions in the membrane equilibrate with the electrolyte (which is the same at either side at open circuit).

## 4. Results and discussions

### 4.1. Simulated pH profile for different flow orientations

The $H^+$ ion concentration profile along the BPM is first obtained through a stepwise mass balance (Equation (8), and then it is converted to the corresponding pH values using Visual MINTEQ, as explained in the SI. The pH profiles at i = 200 mA $cm^{-2}$ and 25 mA $cm^{-2}$ for each flow orientation along the z-axis and the maximum $\Delta pH_{BPM}$ ($= pH_{Base} - pH_{Acid}$) are shown in Fig. 3 and Fig. S2, respectively.

In the co-flow mode (Fig. 3A–C), $\Delta pH^{BPM}_{z=0}$ is equal to zero because the same feed solutions are used at both sides of the BPM. The $\Delta pH_{BPM}$ increases along the z-axis for co-flow mode, and reaches its maximum at z = L. The co-flow mode also creates a higher $\Delta pH^{BPM}_{z=L}$ than the other flow modes, because in single pass co-flow, the highest pH (i.e., alkaline) and lowest pH (i.e., acidic) at either side of the BPM coincide at z = L.

However, for the counter-flow (Fig. 3D–F), $\Delta pH_{BPM}$ at z = 0 is never zero when a current is applied, and $\Delta pH_{BPM}$ at z = L is smaller than that of the co-flow mode. One more important difference between the co-flow (Fig. 3A–C) and counter-flow (Fig. 3D–F) modes is the position of $\Delta pH^{max}_{BPM}$, while in the co-flow mode, $\Delta pH^{max}_{BPM}$ always takes place at z = L, in the counter-flow it can occur near the middle of the cell (depending on the applied current density and solution type). This is particularly visible in poorly buffered solutions (Fig. 3 D).

In buffered solutions such as the phosphate and bicarbonate case, the buffering ions partly neutralize the produced protons and hydroxides. For the phosphate solution, this neutralization is occurring in reactions at three $pK_a$ values:

$$H_3PO_4 \leftrightarrow H^+ + H_2PO_4^-, \quad pKa_1 \sim 2.3$$
$$H_2PO_4^- \leftrightarrow H^+ + HPO_4^{2-}, \quad pKa_2 \sim 7.2$$
$$HPO_4^{2-} \leftrightarrow H^+ + PO_4^{3-}, \quad pKa_3 \sim 12.4$$

The effect of these $pK_a$'s is reflected in the mild slopes (i.e., almost horizontal) when the pH is near one of the $pK_a$'s in Fig. 3 C, F, I.

In the bicarbonate solution, upon acidification, a similar neutralization reaction takes place:

$$HCO_3^- + H^+ \leftrightarrow CO_2(aq) + H_2O$$

However, the buffer effect is less visible in Fig. 3 B, E, H, due to the lower buffering capacity of the bicarbonate solution compared to the phosphate solution in this study (i.e., 2.5 mM vs. 50 mM).

Under a constant current density, the lowest values of $\Delta pH_{BPM}$ can be achieved by recirculating the acidic stream of the BPM to the adjacent base compartment, over the bipolar membrane (Fig. 1 C, D).

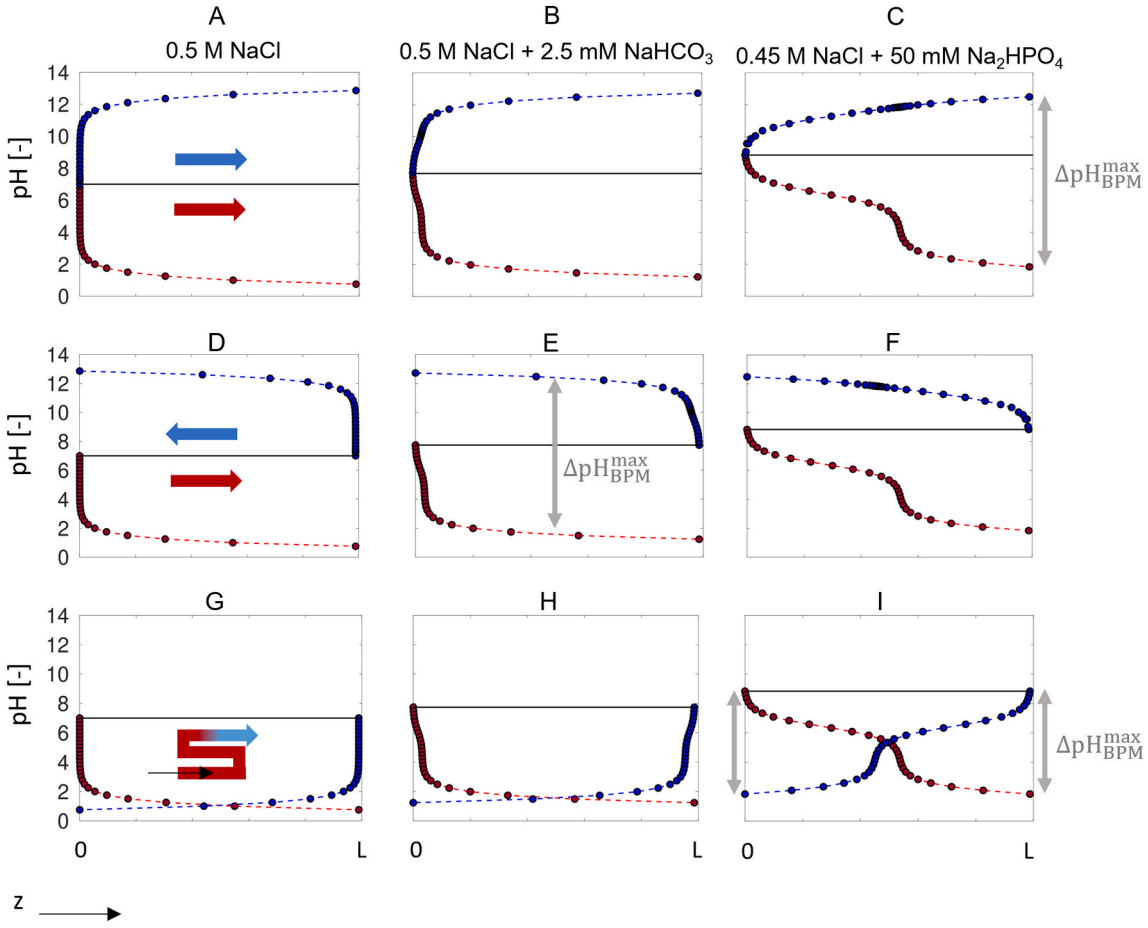


**Fig. 3.** The simulated pH profile along the z-axis, for the co-flow (A, B, C), counter-flow (D, E, F), and co-recirculation (G, H, I), under assumption of a uniform current density of 200 mA $cm^{-2}$ and $t_r$ = 44 s (i.e., flow rate of 30 ml $min^{-1}$). The black horizontal line shows the initial solution pH. Blue and red arrows show flow orientations. Fig. 3 shows the pH profiles for $\frac{i\, t_r}{d}$ = 8800 mC·$cm^{-3}$ = 0.091 mol eq·$L^{-1}$. The counter-recirculation flow is not shown, but it creates $\Delta pH_{BPM} = 0$ for $0 \leq z \leq L$. (For interpretation of the references to colour in this figure legend, the reader is referred to the Web version of this article.)

Recirculation can be useful for resource recovery applications e.g., BPMED $CO_2$ capture/conversion and ammonia recovery.

The co-recirculation mode creates a smaller $\Delta pH_{BPM}$ compared to the co-flow and counter-flow as seen in Fig. 3 G-I. At the extreme, the counter-recirculation flow can even create $\Delta pH_{BPM} = 0$ on every position along the z-axis when no product is extracted in the process.

Flow orientations affect the pH-profile along the BPM and the magnitude of the maximum $\Delta pH_{BPM}$ (Fig. 3); for the co-flow (A, B, C), $\Delta pH_{BPM}^{max}$ is at z = L, while for the co-recirculation (G, H, I), $\Delta pH_{BPM}^{max}$ is much smaller and located at z = 0 and L. For the counter-flow mode (D, E, F), $\Delta pH_{BPM}^{max}$ is at the inside of the cell, and for the counter-recirculation flow mode, $\Delta pH_{BPM}^{max}$ is zero on every position along the z-axis in these idealized conditions.

### 4.2. Effect of flow orientation on simulated $V_{rev}$

To obtain the thermodynamic voltage ($V_{rev}$) that is required to drive the water dissociation reaction (WDR) in the BPM, the maximum pH difference ($\Delta pH_{BPM}^{max}$) must be considered in Equation (1) because the voltage must be sufficient to still drive WDR at this ΔpH. This result follows directly from having a single set of electrodes (i.e., a single stage), and implies that the minimum applied cell voltage is no longer a local variable but is equal for the whole cell and depends on the single position in the cell with the highest $\Delta pH_{BPM}$. If this cell voltage is applied, that voltage is also adequate to enable any lower ΔpH along the whole normalized length. In reality, the current density may not be uniform, which would alter the exact shape of the curves in Fig. 3, but still yield the same $\Delta pH_{BPM}^{max}$ and thus the same reversible cell voltage.

Hence, the simulated reversible voltage for each flow mode is obtained using $\Delta pH_{BPM}^{max}$ in Equation (1), and presented in Fig. 4. To ensure applicability of Equation (1), in the simulation, only current densities higher than the limiting current density of Fumatech BPM are considered ($i_{lim} \sim 2.5$ mA cm$^{-2}$, Fig. S3).

In Fig. 4, the simulated $V_{rev}$ increases as the current density increases because, as expected, a higher current density enables higher $\Delta pH_{BPM}^{max}$. For co-flow, $V_{rev}$ requires a cell voltage between ca. 0.6 – 0.7 V for all solutions to achieve i = 200 mA cm$^{-2}$.

$V_{rev}$ decreases by an increase in the buffer capacity (Fig. 4 from A to C), in particular for low current density (<5 mA cm$^{-2}$ for bicarbonate and <100 mA cm$^{-2}$ for phosphate, all at flow rate of 30 ml min$^{-1}$). These lower reversible membrane voltages are related to the lower $\Delta pH_{BPM}^{max}$ that are obtained at these current densities in a buffered solution.

Finally, the flow orientation strongly affects simulated $\Delta pH_{BPM}^{max}$ and, hence, simulated $V_{rev}$ in these calculations; while the co-flow mode enables the highest $V_{rev}$, the voltage is almost half of that when co-recirculation is used. Assuming no buffer extraction upon recirculating, $V_{rev}$ in the counter-recirculation is equal to zero regardless of the used solutions, at all current densities (green vertical line in Fig. 4).

The difference in simulated $V_{rev}$ between the co-flow and counter-flow is minor for low current densities for unbuffered or poorly buffered solutions (<50 mV difference in Fig. 4 A, B), but increases at i > 100 mA cm$^{-2}$ for buffered phosphate solution (Fig. 4 C). The increased difference for 50 mM phosphate solution is reflected in the pH profile along the z-axis (Fig. 3) and follows from the balance between the moles $H^+$ added (max 88 mM, Fig. 4) and the 2 × 50 mM buffer capacity in the acidic compartment.

### 4.3. Effect of flow orientation on experimental $\Delta pH_{BPM}$ and $V_{BPM}$

The pH-gradient over the BPM at z = 0 and z = L, and the BPM-voltage (at z = 0.5L) were measured in the six-compartment electrochemical cell. Fig. 5 compares the simulated pH-gradients with the measured ones, at the outflow of the alkaline stream. The individual $\Delta pH_{BPM}$ measurements at each current density are shown in Fig. S4.

As expected through the simulations, the co-flow mode creates the highest experimentally obtained $\Delta pH_{BPM}^{max}$ while the counter-recirculation generates the smallest $\Delta pH_{BPM}^{max}$ for all tested solutions (see Fig. S4 for grouping per solution). The values for the counter-flow and co-recirculation orientations are positioned between those of the co-flow and counter-recirculation.

The data points for co-flow, counter-flow and co-recirculation flow are all very close to the 1:1 line. An exception is the simulated vs. measured $\Delta pH_{BPM}$ for 0.5 M NaCl counter-recirculation flow. There, at base outflow (z = 0), the simulations predict a zero-pH difference, while the experiments show a $\Delta pH_{BPM}$ at the outflow of 1–3 pH units (depending on current density) as illustrated in Fig. 5 by the green circles. This is explained from the sensitivity of unbuffered solutions to pH change around neutral pH. Although a pH difference of ~ 3 units might seem significant, around pH = 7, it translates into an $H^+$ ion concentration difference of less than 1 μM. Since in the counter-recirculation mode, the highly acidic stream will come adjacent to a CEM upon recirculation to the base compartment, the $H^+$ ion can exchange with $Na^+$ ion over the CEM due to its concentration gradient toward the adjacent cell (Figs. S5 and 6). A $H^+$ ion transport in the order of 1–2% already can shift the output base pH from 7 to 10, justifying the

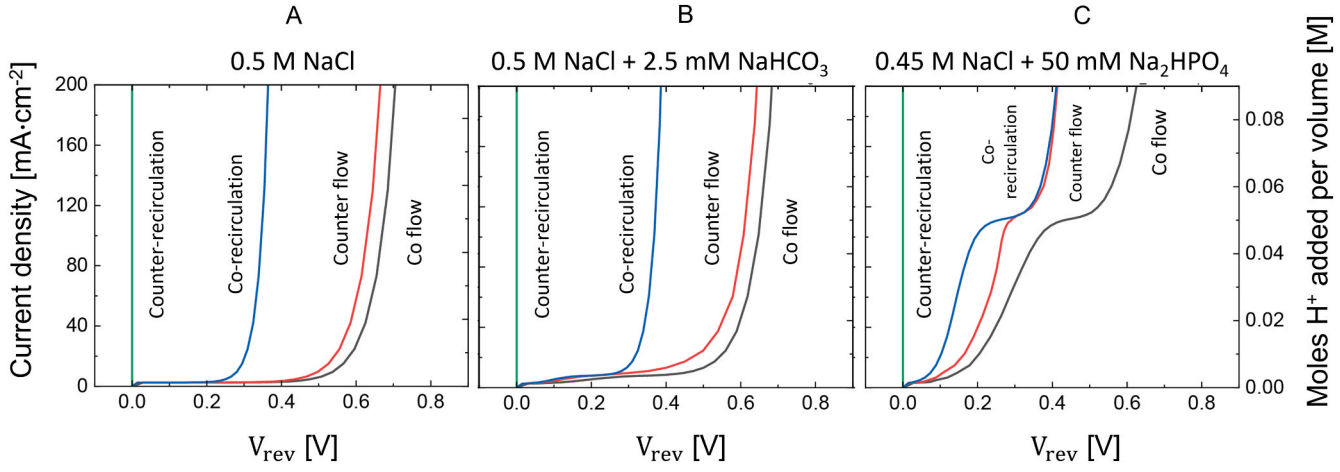


**Fig. 4.** The reversible Nernstian voltage ($V_{rev}$) required to drive the water dissociation reaction at the BPM junction layer at steady state vs. current densities ($i > i_{lim}$) and the corresponding moles of $H^+$ ions added per volume of the solution. Here, "Moles $H^+$ added per volume" represents the produced [$H^+$] from WDR (see Equation (5)). The simulated $\Delta pH_{BPM}^{max}$ has the exact same trend as $V_{rev}$ because $V_{rev} = 0.059\Delta pH_{BPM}^{max}$. In the simulation, same as in the experiments, $t_r$ = 44 s (i.e., flow rate of 30 ml min$^{-1}$) is used.

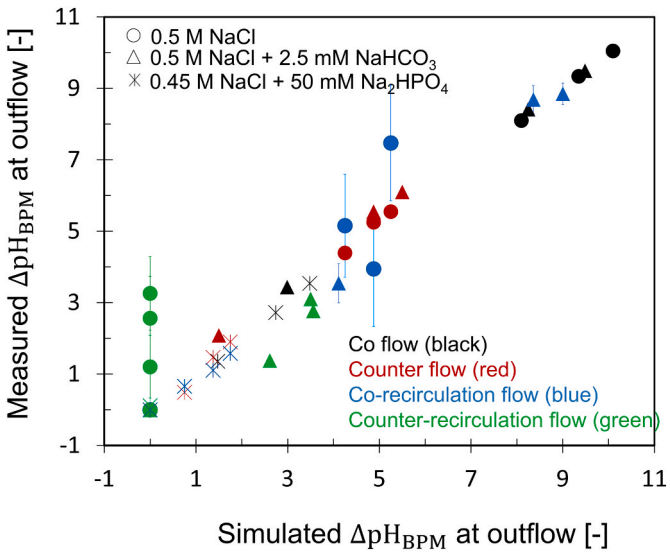


**Fig. 5.** Comparison of the measured and simulated $\Delta pH_{BPM}$ for the three solutions and four flow orientations, at the outflow of the base compartment. For the co-flow and co-recirculation, the "outflow" refers to z = L, while for the counter-flow and counter-recirculation, outflow is at z = 0. All measurements are done at compartment residence time $t_r = 44$ s (i.e., flow rate of 30 ml $min^{-1}$). Error bars indicate the standard error. For data points without error bar, the error bars are smaller than the symbols. For 0.5 M NaCl, from lowest to highest current density, ΔpH measurements fluctuate within ranges of (0.1–2.4), (1.6–4), (1.1–4.5) for counter-recirculation and (2.7–7.7), (2.1–6.5), (3.3–9.2) for co-recirculation modes, respectively.

discrepancy in Fig. 5- green circles. The unstable base outflow pH measurements for recirculation flow modes of 0.5 M NaCl (Figure S5 C-D) are another sign of such hydrogen ions transport taking place, reflected in relatively large error bars for the counter- and co-recirculation of NaCl (blue and green circles in Fig. 5).

This discrepancy for counter-recirculation disappears when a buffer is present; the experimentally obtained $\Delta pH_{BPM}$ is (as simulated) very close to zero for the phosphate buffered solution. For the bicarbonate solution in Fig. 5, $CO_2$ (aq) extraction from the acidic compartment is done (via a membrane contactor) prior to recirculation to the base compartment in experiments as well as in simulations. Upon such degassing, the buffer capacity decreases.

The close agreement between the simulated and experimental values in Fig. 5 shows that the theoretical framework in Equations (3)–(8) is adequate for defining the pH profile. Furthermore, with most data points so close to the 1:1 diagonal, the actual BPM-coulombic efficiency is close to 100% (as assumed in the simulations) for our cases, regardless of the flow orientation. The experiments results, also, confirm that the pH difference over the BPM is indeed heavily dependent on the flow orientation.

Following the theoretical framework, we expect to see a reversible membrane voltage that is proportional to the $\Delta pH_{BPM}$. However, the experimentally measured reversible membrane voltage $V_{rev}$, determined according to the current-interrupt method, is not affected at all by the flow orientation for any of the tested solutions (Fig. 6 B). In more detail, as the applied current density increases, $V_{rev}$ increases but reaches a plateau (<0.8 V) already at (or below) 5 mA $cm^{-2}$, while $V_{irr}$ keeps increasing (NaCl example in Fig. 6 A and other solutions in Figs. S7–8 - Table S2). Hence, even though a clear difference in $\Delta pH_{BPM}^{max}$ is measured between the cases (Fig. 5), the reversible voltage ($V_{rev}$) and the irreversible losses ($V_{irr}$) are virtually independent of the flow orientation, for all current densities $\geq$ 5 mA $cm^{-2}$ and for all solutions (Table S2). This absence of any impact of the flow orientation on $V_{rev}$ is remarkable, because, theoretically, when the water dissociation reaction is the dominant, a difference of ~ 6 pH units in $\Delta pH_{BPM}^{max}$ should enable a $6 \times 0.059 = 354$ mV difference in $V_{rev}$. However, that is not observed in the experimental results (Fig. 6 B).

Instead, from Fig. 6 (and Table S2), we see that the experimentally obtained reversible voltage ($V_{rev}$) are.

1. Higher than simulated values (up to six times)
2. Lower than 0.83 V, with values between ca. 0.59–0.74 V depending on the applied current density and feed solution.

The insignificant effect of flow orientation on the reversible voltage implies that, when the water dissociation reaction in the BPM is at substantial rate (i.e., i $\geq$ 5 mA $cm^{-2}$ and higher), the effect of the solution-pH gradient on BPM-voltage is dwarfed. Furthermore, because all cases have similar $V_{rev}$ values regardless of the difference in solutions and flow orientations, the origin of this similarity in $V_{rev}$ must come from one thing that is kept the same among the cases: the bipolar membrane itself.

Since the reversible voltage for extreme pH gradient (14 units) is ca. 0.826 V, and the obtained voltages are between 0.59 and 0.74 V, there is some pH-jump at the membrane-electrolyte interface, or there is a pH gradient over the CEL-AEL interface that is smaller than 14 units. When a pH-jump at the membrane-electrolyte interface would occur, e.g. a higher proton concentration in the CEL than in the electrolyte facing the CEL, the Donnan potential at this interface partly counteracts the water

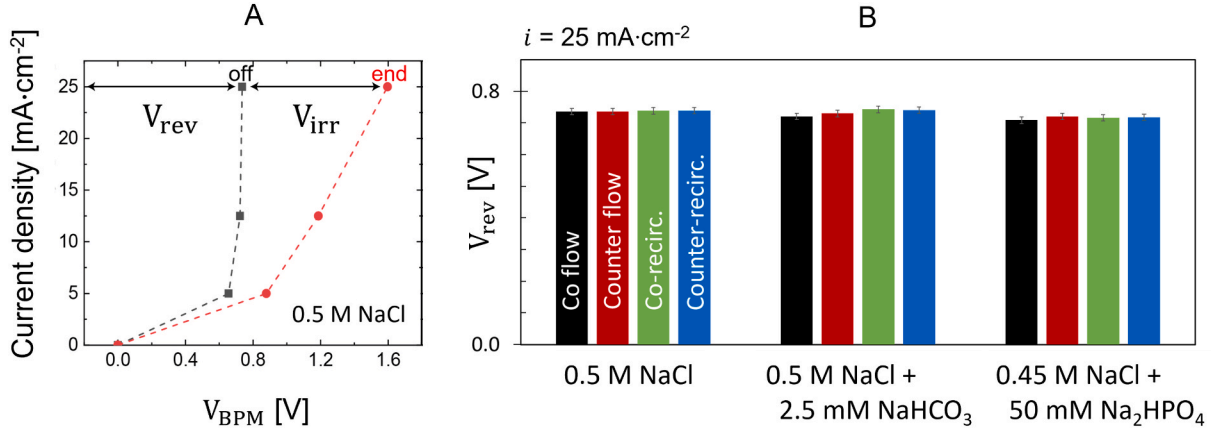


**Fig. 6.** A) Characteristic current–voltage curves from chronopotentiometry, showing the measured steady state BPM-voltage vs. the applied current density for the co-flow in 0.5 M NaCl. $V_{rev}$ and $V_{irr}$ are gathered from "Switch-off" potential after constant current for 20 min with indicated current densities (Fig. S7). Here, $V_{irr}$ include both the BPM and solution resistances. B) The measured reversible voltage for all solutions (at 25 mA $cm^{-2}$) using flow rate of 30 ml $min^{-1}$ ($t_r$ = 44 s).

dissociation voltage [5]. Keeping the local solution pH near-neutral (e.g. minimizing concentration polarization), and keeping the CEL pH low/AEL pH high, would further exploit this effect. This would require a bipolar membrane that is prone to internal concentration polarization (e.g. having very thin layers or high affinity to protons and hydroxides over other ions) and flow geometries to keep the local pH close to the bulk pH.

The situation of a mild pH gradient over the CEL-AEL interface is more complex. As for internal properties of the BPM that affect its voltage for WDR, the type and thickness of the BPM-catalyst layer is reported to be crucial [26–28,44]. It is shown that the local pH in the junction layer of the BPM affects the activity of the catalyst [28], but that, unfortunately, the currently developed catalysts are only activated at high (local) pH-gradient. Furthermore, the internal ion concentration profiles in the BPM layers show a large gradient (i.e., internal concentration polarization), especially under high applied current [27]. This internal concentration polarization increases the pH gradient at the BPM catalyst layer and thereby the catalytic WDR, but also increases the thermodynamically required potential to dissociate water. If new catalysts with ability to perform at close to neutral pH are developed, a decrease in the internal pH-gradient can decrease the WDR-voltage. In addition, thin catalyst layers (i.e., ~100–200 nm) are expected to decrease the BPM-voltage under WDR-dominated regime [28].

### 4.4. Irreversible losses ($V_{irr}$)

The irreversible voltage losses, $V_{irr}$, are compared for all flow orientations and for all solutions. Also, here, the total $V_{irr}$ increases with the applied current density for all solutions (Fig. 7), but no significant difference is observed in the magnitude of $V_{irr}$ between the different flow orientations (Table S2). The different solutions have, however, a slight impact on $V_{irr}$, as demonstrated in Fig. 7.

Fig. 7 shows that $V_{irr}$ increases with the buffering capacity of the solution. The solution resistivity ($R_{sol}$) is similar for all the tested solutions (ca. 0.95–0.98 Ω, Table S1 and Equations S(1) and (2)), and it remains unchanged for $2 < pH < 12$. Therefore, the BPM-contribution to the irreversible losses ($V_{irr}^{BPM}$) can be calculated (Fig. 7, dashed lines).

In the BPM, the initial equilibrium resistance ($R_{mem,\ ini}$ in Equation (9)) is different than the steady state (i.e., transport-state) resistance ($R_M$ in Equation (2)-Table S3) [43]. Both resistances change with current density, membrane history and electrolyte solutions. In this work, the membrane transport-state resistivity ($R_M$) is measured to be ~ 13–31 Ω $cm^2$ $R_M$ decreases with current density, while increases with buffer capacity (Fig. S9). The latter is probably because of the lower conductivity of AEL and CEL layers due to the presence of buffer in them.

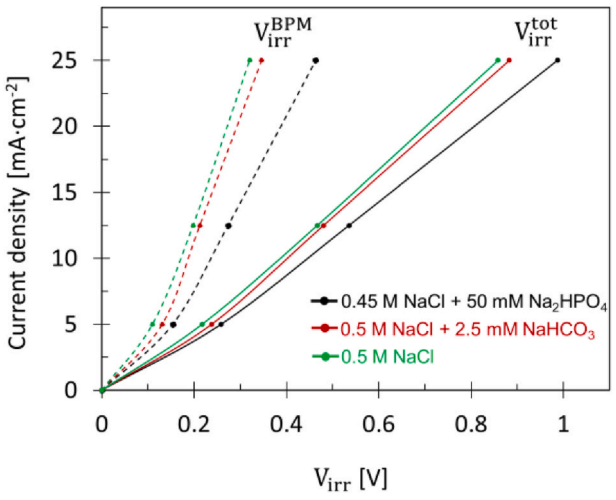


**Fig. 7.** The total irreversible voltage ($V_{irr}^{tot}$) vs. the applied current density (solid lines). Tested solutions are 0.5 M NaCl (green), 0.5 M NaCl + 2.5 mM $NaHCO_3$ (red), and 0.45 M NaCl + 50 mM $Na_2HPO_4$ (black). $t_r = 44$ is applied for all cases. By correcting for the solution resistivity ($V_{irr}^{sol}$, between the two sides of the membrane and the tips of the reference electrodes: Equations S(1) and (2)), values of $V_{irr}^{BPM}$ (Equation (2), dashed line) can be obtained as $V_{irr}^{tot} \sim V_{irr}^{BPM} + V_{irr}^{sol}$. (For interpretation of the references to colour in this figure legend, the reader is referred to the Web version of this article.)

At applied current density of 25 mA $cm^{-2}$, $V_{irr}^{BPM}$ contributes to ~ 37 % (for 0.5 M NaCl), 39 % (for 0.5 M NaCl + 2.5 mM $NaHCO_3$), and 47 % (for 0.45 M NaCl + 50 mM $Na_2HPO_4$) of the total measured irreversible voltage ($V_{irr}^{tot}$), respectively (Fig. 7). The remaining contribution is mainly due to the solution resistivity between the reference electrodes and the membrane (Equations S1 and S2), which unfortunately, even using the micro-reference electrodes, is rather high compared to the membrane resistivity.

In addition to the higher $R_M$, $\eta_{WDR}$ can also play a role in justifying the slightly higher $V_{irr}^{BPM}$ of the phosphate solution compared to 0.5 M NaCl (Equation (2)). It is recently shown that $\eta_{WDR}$ strongly depends on the local pH in the BPM junction layer (JL) [28,40]. The existence of the phosphate buffer inside the BPM layers can change the local pH at the JL, affecting the WDR catalyst activity compared to the unbuffered 0.5 M NaCl solution. Unfortunately, the WDR catalyst's properties of the used Fumasep BPM are unknown, and, thus, further investigations on the effect of local pH on activity of the WDR catalyst is beyond the scope of this work.

## 5. Conclusion

In this work, with the aim of decreasing the energy consumption of bipolar membrane (BPM) based applications, the effect of pH gradient ($\Delta pH_{BPM}$) on the reversible and irreversible voltage components associated with the BPM is investigated. The pH dependency is studied through an analytical model and is also measured experimentally, for four flow orientations using buffered and unbuffered electrolytes. First, using the analytical model, the pH profile along the BPM (i.e., in the flow direction) is obtained for each flow orientation. The simulated results fit the experimentally obtained $\Delta pH_{BPM}$ at the outflow very well. Second, based on the simulated pH profile, for each flow orientations, the reversible voltage ($V_{rev}$) is modeled. Surprisingly, except for the co-flow mode, the experimentally measured $V_{rev}$ were higher (up to six times) than what was simulated. The origin of this discrepancy is the difference between the bulk and local pH; the local pH at the BPM-electrolyte interface and BPM junction layer (JL) determines the measured $V_{rev}$. However, the (measured) bulk pH is not representative of this local pH. Our results show that, although changing the flow orientations alters $\Delta pH_{BPM}$, it does not affect $V_{rev}$, $V_{irr}$, and $V_{BPM}$. It seems that, when the water dissociation reaction (WDR) dominates, the membrane internal properties overshadow the effect of the bulk $\Delta pH_{BPM}$. Therefore, to decrease the BPM-voltage (thus its energy consumption) under WDR regime, focus must be shifted towards tuning the membrane properties (e.g., WDR catalyst and thickness) rather than the external pH profile along the membrane.

## Author statement

R. Sharifian did Investigation (experiments and simulations), Conceptualization, Analysis, Visualization and Writing Original Draft, M.A. Blommaert did Validation and Review & Editing, M. Bremer did Investigation, R.M. Wagterveld did Supervision and Review & Editing and D.A. Vermaas did Conceptualization, Supervision, Review & Editing and Funding acquisition.

## Declaration of competing interest

The authors declare that they have no known competing financial

interests or personal relationships that could have appeared to influence the work reported in this paper.

## Acknowledgements

This work was performed in the NWO-cooperation framework of Wetsus, Centre of Excellence for Sustainable Water Technology (www.wetsus.nl). Wetsus is funded by the Dutch Ministry of Economic Affairs, the European Union Regional Development Fund, the Province of Fryslân, the City of Leeuwarden and the EZ/Kompas program of the Samenwerkingsverband Noord-Nederland". The authors like to thank the participants of the research theme "Concentrates" in Wetsus and research group "Transport phenomena" in faculty of applied sciences at TU Delft for the discussions and their (financial) support. This research received funding from the Netherlands Organization for Scientific Research (NWO) in the framework of the project ALW.2016.004.

## Appendix A. Supplementary data

Supplementary data to this article can be found online at https://doi.org/10.1016/j.memsci.2021.119686.

## References

[1] M.A. Ali, M. Rakib, S. Laborie, P. Viers, G. Durand, Coupling of bipolar membrane electrodialysis and ammonia stripping for direct treatment of wastewaters containing ammonium nitrate, J. Memb. Sci. 244 (Nov. 2004) 89–96.
[2] J. Balster, I. Punt, D. Stamatialis, H. Lammers, A.B. Verver, M. Wessling, Electrochemical acidification of milk by whey desalination, J. Memb. Sci. 303 (Oct. 2007) 213–220.
[3] L. Bazinet, F. Lamarche, D. Ippersiel, Bipolar-membrane electrodialysis: applications of electrodialysis in the food industry, Trends Food Sci. Technol. 9 (3) (1998) 107–113.
[4] D.A. Vermaas, W.A. Smith, Synergistic electrochemical CO2 reduction and water oxidation with a bipolar membrane, ACS Energy Lett. 1 (6) (2016) 1143–1148.
[5] D.A. Vermaas, S. Wiegman, T. Nagaki, W.A. Smith, Ion transport mechanisms in bipolar membranes for (photo)electrochemical water splitting, Sustain. Energy Fuels 2 (9) (2018) 2006–2015.
[6] M.B. McDonald, M.S. Freund, Graphene oxide as a water dissociation catalyst in the bipolar membrane interfacial layer, ACS Appl. Mater. Interfaces 6 (16) (2014) 13790–13797.
[7] N.M. Vargas-Barbosa, G.M. Geise, M.A. Hickner, T.E. Mallouk, Assessing the utility of bipolar membranes for use in photoelectrochemical water-splitting cells, ChemSusChem 7 (11) (Nov. 2014) 3017–3020.
[8] J. Luo, D.A. Vermaas, D. Bi, A. Hagfeldt, W.A. Smith, M. Grätzel, Bipolar membrane-assisted solar water splitting in optimal pH, Adv. Energy Mater. 6 (13) (2016) 1600100.
[9] D.A. Vermaas, M. Sassenburg, W.A. Smith, Photo-assisted water splitting with bipolar membrane induced pH gradients for practical solar fuel devices, J. Mater. Chem. A 3 (38) (2015) 19556–19562.
[10] D.A. Vermaas, W.A. Smith, Chapter 8 applications of bipolar membranes for electrochemical and photoelectrochemical water splitting. In *Advances in Photoelectrochemical Water Splitting: Theory, Experiment and Systems Analysis*, The Royal Society of Chemistry, 2018, pp. 208–238.
[11] A.T. Emrén, V.J.M. Holmström, Energy storage in a fuel cell with bipolar membranes burning acid and hydroxide, Energy 8 (4) (1983) 277–282.
[12] W.J. van Egmond, M. Saakes, I. Noor, S. Porada, C.J.N. Buisman, H.V.M. Hamelers, Performance of an environmentally benign acid base flow battery at high energy density, Int. J. Energy Res. 42 (4) (2018) 1524–1535.
[13] F. Ilhan, H.A. Kabuk, U. Kurt, Y. Avsar, H. Sari, M.T. Gonullu, Evaluation of treatment and recovery of leachate by bipolar membrane electrodialysis process, Chem. Eng. Process. Process Intensif. 75 (2014) 67–74.
[14] M.D. Eisaman, L. Alvarado, D. Larner, P. Wang, B. Garg, K.A. Littau, CO $_2$ separation using bipolar membrane electrodialysis, Energy Environ. Sci. 4 (4) (2011) 1319–1328.
[15] S. Datta, et al., Electrochemical CO $_2$ capture using resin-wafer electrodeionization, Ind. Eng. Chem. Res. 52 (43) (2013) 15177–15186.
[16] A. Iizuka, K. Hashimoto, H. Nagasawa, K. Kumagai, Y. Yanagisawa, A. Yamasaki, Carbon dioxide recovery from carbonate solutions using bipolar membrane electrodialysis, Sep. Purif. Technol. 101 (2012) 49–59.
[17] M. Eisaman, et al., Energy-efficient electrochemical CO2 capture from the atmosphere, Tech. Proc. (2009) 5–8. Clean Technol. Conf. Trade Show.
[18] M. Shuangchen, H. Tingting, M. Lan, M. Jingxiang, C. Gongda, Y. Jing, Experimental study on desorption of simulated solution after ammonia carbon capture using bipolar membrane electrodialysis, Int. J. Greenh. Gas Control 42 (2015) 690–698.
[19] C.F. de Lannoy, et al., Indirect ocean capture of atmospheric CO2: Part I. Prototype of a negative emissions technology, Int. J. Greenh. Gas Control 70 (May) (2018) 243–253.
[20] Y. Zhang, I. Angelidaki, Recovery of ammonia and sulfate from waste streams and bioenergy production via bipolar bioelectrodialysis, Water Res. 85 (2015) 177–184.
[21] E. Koivisto, R. Zevenhoven, Energy use of flux salt recovery using bipolar membrane electrodialysis for a CO2 mineralisation process, Entropy 21 (4) (2019).
[22] N. van Linden, G.L. Bandinu, D.A. Vermaas, H. Spanjers, J.B. van Lier, Bipolar membrane electrodialysis for energetically competitive ammonium removal and dissolved ammonia production, J. Clean. Prod. 259 (2020) 120788.
[23] M.B. McDonald, S. Ardo, N.S. Lewis, M.S. Freund, Corrigendum: use of bipolar membranes for maintaining steady-state pH gradients in membrane-supported, solar-driven water splitting, ChemSusChem 8 (1) (Jan. 2015) 14.
[24] S.Z. Oener, S. Ardo, S.W. Boettcher, Ionic processes in water electrolysis: the role of ion-selective membranes, ACS Energy Lett. 2 (11) (Nov. 2017) 2625–2634.
[25] M. Lin, L. Han, M.R. Singh, C. Xiang, An experimental- and simulation-based evaluation of the CO2 utilization efficiency of aqueous-based electrochemical CO2 reduction reactors with ion-selective membranes, ACS Appl. Energy Mater. 2 (8) (Aug. 2019) 5843–5850.
[26] R. Pärnamäe, et al., Bipolar membranes: a review on principles, latest developments, and applications, J. Memb. Sci. 617 (2021) 118538.
[27] J.C. Bui, I. Digdaya, C. Xiang, A.T. Bell, A.Z. Weber, Understanding multi-ion transport mechanisms in bipolar membranes, ACS Appl. Mater. Interfaces 12 (47) (2020) 52509–52526.
[28] S.Z. Oener, M.J. Foster, S.W. Boettcher, Accelerating water dissociation in bipolar membranes and for electrocatalysis, Science 80 (2020) eaaz1487.
[29] P. Ramírez, S. Mafé, J.A. Manzanares, J. Pellicer, Membrane potential of bipolar membranes, J. Electroanal. Chem. 404 (2) (1996) 187–193.
[30] J. Veerman, M. Saakes, S.J. Metz, G.J. Harmsen, Electrical power from sea and river water by reverse electrodialysis: a first step from the laboratory to a real power plant, Environ. Sci. Technol. 44 (23) (2010) 9207–9212.
[31] D.A. Vermaas, J. Veerman, N.Y. Yip, M. Elimelech, M. Saakes, K. Nijmeijer, High efficiency in energy generation from salinity gradients with reverse electrodialysis, ACS Sustain. Chem. Eng. 1 (10) (2013) 1295–1302.
[32] R. Sharifian, R.M. Wagterveld, I.A. Digdaya, C. Xiang, D.A. Vermaas, Electrochemical carbon dioxide capture to close the carbon cycle, " *Energy Environ. Sci.*, 2021.
[33] L. Shi, L. Xiao, Z. Hu, X. Zhan, Nutrient recovery from animal manure using bipolar membrane electrodialysis: study on product purity and energy efficiency, Water Cycle 1 (2020) 54–62.
[34] H. Strathmann, H.J. Rapp, B. Bauer, C.M. Bell, Theoretical and practical aspects of preparing bipolar membranes, Desalination 90 (1–3) (1993) 303–323.
[35] K. Sun, R. Liu, Y. Chen, E. Verlage, N.S. Lewis, C. Xiang, A stabilized, intrinsically safe, 10% efficient, solar-driven water-splitting cell incorporating earth-abundant electrocatalysts with steady-state pH gradients and product separation enabled by a bipolar membrane, Adv. Energy Mater. 6 (13) (2016) 1–7.
[36] M.A. Blommaert, D.A. Vermaas, B. Izelaar, B. In't Veen, W.A. Smith, Electrochemical impedance spectroscopy as a performance indicator of water dissociation in bipolar membranes, J. Mater. Chem. A 7 (32) (2019) 19060–19069.
[37] H. Strathmann, J.J. Krol, H.J. Rapp, G. Eigenberger, Limiting current density and water dissociation in bipolar membranes.pdf, J. Memb. Sci. 125 (1997) 123–142.
[38] R. El Moussaoui, G. Pourcelly, M. Maeck, H.D. Hurwitz, C. Gavach, Co-ion leakage through bipolar membranes Influence on I-V responses and water-splitting efficiency, J. Memb. Sci. 90 (3) (1994) 283–292.
[39] F.G. Wilhelm, N.F.A. Van Der Vegt, H. Strathmann, M. Wessling, Current-voltage behaviour of bipolar membranes in concentrated salt solutions investigated with chronopotentiometry, J. Appl. Electrochem. 32 (4) (2002) 455–465.
[40] S.Z. Oener, L.P. Twight, G.A. Lindquist, S.W. Boettcher, Thin cation-exchange layers enable high-current-density bipolar membrane electrolyzers via improved water transport, ACS Energy Lett. (1–8) (2020).
[41] A. Alcaraz, P. Ramírez, S. Mafé, H. Holdik, B. Bauer, Ion selectivity and water dissociation in polymer bipolar membranes studied by membrane potential and current-voltage measurements, Polymer (Guildf). 41 (17) (2000) 6627–6634.
[42] M.D. Eisaman, L. Alvarado, D. Larner, P. Wang, K.A. Littau, CO 2 desorption using high-pressure bipolar membrane electrodialysis, Energy Environ. Sci. 4 (10) (2011) 4031–4037.
[43] F.G. Wilhelm, N.F.A. Vegt, M. Wessling, H. Strathmann, Chronopotentiometry for advanced current-voltage characterization of bipolar membranes, J. Electroanal. Chem. 502 (2001) 152–166.
[44] E. Al-Dhubhani, et al., Entanglement-enhanced water dissociation in bipolar membranes with 3D electrospun junction and polymeric catalyst, ACS Appl. Energy Mater., Mar. 4 (4) (2021) 3724–3736, https://doi.org/10.1021/acsaem.1c00151.